Simultaneous Particle Image Velocimetry and Schlieren Measurements of Slow-burning Flames†

C. Schwenzer*[1], R. Hesse[1], R. Glaznev[1], V. I. Babushok[2], G. T. Linteris[2], H. Pitsch[1], and J. Beeckmann[1]

[1]Institute for Combustion Technology, RWTH Aachen University, Templergraben 64, 52056 Aachen, Germany
[2]National Institute of Standards and Technology, Gaithersburg, MD, USA

Abstract

Laminar flame speed is a key parameter in understanding a fuel's combustion behavior and is used to optimize chemical kinetic mechanisms, simulate combustion processes, and classify fire hazardous potential. One commonly used method to extract laminar flame speed is by combusting premixed fuel-oxidizer-mixtures in a spherical vessel and capturing the propagating flame with a high-speed camera. However, some substances burn at low flame speeds and are affected by buoyancy, leading to a deformed flame and unique Markstein effects. In this study, we used the Schlieren method and Particle Image Velocimetry to measure flames of methane-air mixtures, cross-validating both laminar flame speed measurement techniques. For a very lean methane/air mixture, it was found that because of the observed negative Markstein length, the local curvature promotes the formation of a mushroom-shaped flame.

Introduction

Laminar flame speed is a fundamental characteristic of combustion that refers to the speed at which a flame front propagates through a fuel-air mixture under laminar flow conditions [1]. It is used in many applications, e.g., to optimize chemical kinetic mechanisms, to simulate combustion processes, and to classify hazardous fire potential [2]. Among the large variety of methods to extract the laminar flame speed experimentally, the combustion of premixed fuel-oxidizer-mixtures in a spherical combustion vessel is widely used because of its flexibility in temperature, pressure, and fuel. Herein, the laminar flame speed can be obtained by capturing the propagating flame with a high-speed camera through an optically accessible combustion vessel [3]. While highly reactive mixtures generally burn fast and produce a spherical flame front, some substances, such as diluted fuels and refrigerants with a low global warming potential, burn at low flame speeds and are affected by buoyancy [4]. As a result, the flame is deformed eventually leading to a mushroom shape. Consequently, unique Markstein effects produced by locally varying curvature and strain rates along the flame front arise which have been only scarcely studied in the literature [5]. The impact of buoyancy can be described by the Richardson number Ri, defined as

$$\mathrm{Ri} = \left(1 - \frac{\rho_\mathrm{b}}{\rho_\mathrm{u}}\right) \frac{g R_\mathrm{f}}{\dot{R}_\mathrm{f}^2}. \tag{1}$$

Here, ρ_u and ρ_b are the density in the unburned and burned gas, g is the gravitational acceleration, R_f is the flame radius, and $\dot{R}_\mathrm{f}$ refers to the propagation speed of the flame front in the laboratory flame [6]. The Richardson number indicates whether flame propagation is driven more by fractions of gravitationally induced buoyancy ($\mathrm{Ri} > 1$) or by the laminar flame speed itself and thus by chemical energy release ($\mathrm{Ri} < 1$) [6]. Sufficiently slow flames have Richardson numbers larger than unity and are buoyant. In a numerical study by Berger et al. [5], a methane/air flame at standard thermodynamic conditions and an equivalence ratio of $\phi = 0.5$ was investigated for buoyancy effects. They showed that the Richardson number starts low and increases with time while the flame becomes larger. The flame appears spherical up to $\mathrm{Ri} \approx 3$. At $\mathrm{Ri} = 3.5$, a visible cusp begins to form at the bottom of the flame that grows over time. This is also represented by the increasing Richardson number reaching values of 15. The change in the flame shape due to buoyancy makes allocating a singular instantaneous propagation speed difficult. Therefore, the flame propagation speed with respect to the flame surface location is needed. This requires knowledge of the local curvature and strain, which cannot be determined in a regular Schlieren experiment. Therefore, Particle Image Velocimetry (PIV) is used to determine the flow field around the flame to calculate a local flame propagation speed.

The aim of the experimental investigation of buoyancy effects in laminar flames is to gain a better understanding of the underlying mechanisms that drive flame deformation under such conditions. The results of this investigation can be used to develop more accurate flame propagation models and optimize combustion processes in various applications.

Experimental Framework

The experiments were performed in a closed-vessel utilizing a combined Schlieren and Particle Image Ve-

*Corresponding author: c.schwenzer@itv.rwth-aachen.de

Proceedings of the European Combustion Meeting 2023

locimetry setup, comparable that detailed by Beeckmann et al. [7]. Both the Schlieren and the PIV method allow for the observation of flame front progression. Fig. 1 illustrates the experimental setup schematically, which consists of a spherical combustion vessel with an internal diameter of 100 mm. Sapphire crystal windows with a diameter of 50 mm are located on opposing sides of the vessel. To enable the simultaneous use of the PIV and Schlieren systems, a cylindrical spacer with a width of 30 mm is placed between the two halves of the sphere. This spacer includes two rectangular windows made from sapphire crystals located on opposite sides, with optical access measuring 45 mm in height and 10 mm in width.

The Schlieren setup captures images of the outward displacement of the propagating flame using a dual-field-lens Schlieren configuration [8]. A high-speed CMOS camera (LaVision HighSpeed-Star 6) is paired with this system to capture images at a rate of 5000 frames per second (fps), with a full frame resolution of 1024x1024 pixels, an exposure time of 1/82000 s, and a pixel size of 0.0786 mm/pixel. The Schlieren system is comprised of a continuous high-power LED light source (Luminus CBT-120-R-C11-HM101, BM-R5 [9]), which emits red light with a dominant wavelength of 622 nm.

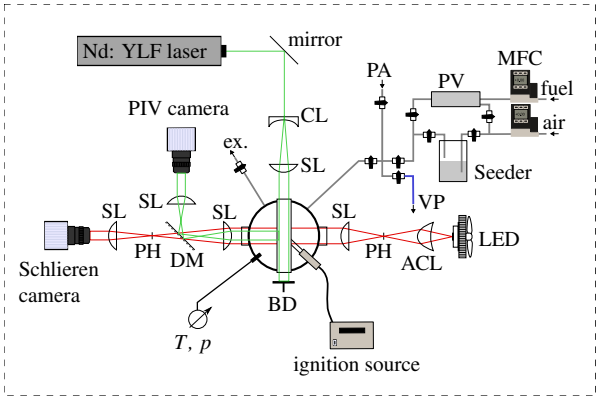

Figure 1: Schematic of the combined Schlieren/PIV experimental setup. SL: spherical lens, ACL: aspherical condenser lens, CL: cylindrical lens, DM: dichroic mirror PH: pinhole, SV: spherical vessel, LED: light-emitting diode, Nd:YLF laser: neodymium-doped yttrium lithium fluoride laser, BD: beam dump, ex: exhaust, PV: premixing vessel, p: pressure sensor, T: temperature sensor, MFC: mass flow controller, VP: vacuum pump, PA: pressurized air.

The PIV setup uses a double-head, high-speed Nd:YLF laser (Litron LDY303HE) to illuminate seeding particles. The laser emits green light at a wavelength of 527 nm with a power output of 35.1 W at 5 kHz. The two cavities are run simultaneously to prevent shot-to-shot intensity variations of each cavity. The laser sheet is created by combining a cylindrical and spherical lens (cf. green light path in Fig. 1). The PIV camera captures the Mie scattering signal from particles via a dichroic mirror with a green light reflection efficiency greater than 90 %. An interferential band-pass filter (527 $\pm$ 10 nm) mounted in front of the camera lens removes any flame chemiluminescence as well as residual red light from the LED. The PIV camera captures images at 5000 fps with a full frame resolution of 1024x1024 pixels, an exposure time of 1/30000 s, and a pixel size of 0.0373 mm/pixel. The spatial resolution of the PIV setup must be high to capture the particle movement effectively. Silicon oil droplets are introduced into the combustion vessel to create seeding for PIV imaging. These droplets have a boiling point temperature of approximately 580 K, which allows them to exist in the preheat zone, capturing the upstream maximum velocity point. This is crucial to measure the unburned flow velocity ahead of the flame [10]. The mixture used in the experiment is supplied from gas cylinders that are connected to two mass flow controllers (MFC), which supply air and fuel separately. The sum of the flow rate from the MFCs is 19 standard liters per minute. To ensure homogeneous mixing, fuel and air are run through a premixing vessel before entering the chamber. For PIV measurements, the airflow is run through a seeder containing silicon oil. The mixture is then run through the chamber for approximately 5 minutes to ensure sufficient amount of seeding particles. An extended spark plug with a diameter of 1 mm is utilized in a two-step ignition system to ignite the mixture at the center of the vessel. Example images of both optical acquisition techniques are given in Fig. 2.

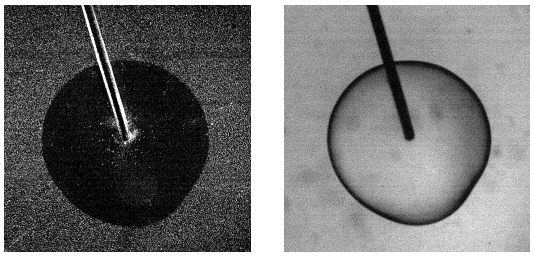

Figure 2: Example PIV image (left) and Schlieren image (right) of a methane/air flame at $p_0 = 101.3\,\mathrm{kPa}$, $T_0 = 298\,\mathrm{K}$, and $\phi = 1.0$.

Flame Dynamics

The flame propagation speed with respect to the laboratory frame $\dot{R}_\mathrm{f} = \mathrm{d}R_\mathrm{f}/\mathrm{d}t$ is the sum of the laminar flame speed S_L and the normal flow velocity V [1]:

$$\dot{R}_\mathrm{f} = V + S_\mathrm{L}. \tag{2}$$

Curvature and strain affect the flame shape. The curvature of the flame front κ is given by

$$\kappa = \nabla \cdot \mathbf{n}, \tag{3}$$

where $\mathbf{n}$ is the normal vector of the flame front pointing toward the burned gas. The strain rate K_S is denoted by

$$K_\mathrm{S} = -\mathbf{n} \cdot \bar{\bar{S}} \cdot \mathbf{n} + \nabla \cdot \mathbf{v}, \tag{4}$$

where $\bar{\bar{S}}$ represents the strain rate tensor. The flame stretch K is the combined effect of curvature and strain rate [11] and reads

$$K = S_L \kappa + K_S. \tag{5}$$

For a spherically expanding flame, K can be simplified to

$$K = \frac{1}{A}\frac{dA}{dt} = \frac{2}{R_f}\dot{R}_f. \tag{6}$$

The Markstein length of stretch $\mathscr{L}_K$ can be used to extrapolate to unstretched conditions (indicated by superscript 0). Then the following linear relationship can be applied:

$$S_L = S_L^0 - \mathscr{L}_K K. \tag{7}$$

Nonlinear extrapolation can be done with the method by Kelley et al. [12]:

$$\left(\frac{S_L}{S_L^0}\right)^2 \ln\left(\frac{S_L}{S_L^0}\right)^2 = -\frac{2\mathscr{L}_K}{S_L^0}\left(\frac{dS_L}{dR_f} - K\right). \tag{8}$$

For buoyant non-spherical flames, there are two Markstein lengths $\mathscr{L}_\kappa$ and $\mathscr{L}_{K_S}$ for the curvature and strain rate. The separation into two independent Markstein lengths was introduced by Clavin et al. [13], yielding

$$S_L = S_L^0 - \mathscr{L}_{K_S} K_S - \mathscr{L}_\kappa S_L^0 \kappa. \tag{9}$$

These equations are valid for the unburned and burned side of the flame front. For a fast-burning flame, the flow velocity in the burned region V_b is assumed zero due to symmetry. The exact flow velocity in the burned V_b is always unknown because the seeding particles evaporate. Applying mass continuity, the laminar flame speed in the unburned then yields

$$S_{L,u} = \rho_b/\rho_u S_{L,b}. \tag{10}$$

This relationship is necessary to determine $S_{L,u}$ with the Schlieren method. With the addition of PIV, Eq. 2 can be applied to determine $S_{L,u}$ by measuring the flow velocity in the unburned V_u.

Results and Discussion

Flame morphology and buoyancy effect

In this study, we investigated two cases with different initial conditions. The first case involved a spherically expanding methane/air flame with initial conditions of $T_0 = 298\,K$, $p_0 = 101.3\,kPa$, and an equivalence ratio of $\phi = 1.0$. The second case involved a slow-propagating buoyant methane/air flame with initial conditions of $T_0 = 298\,K$, $p_0 = 200\,kPa$, and $\phi = 0.6$. Fig. 3 presents sequences of Schlieren imaging for both cases. The top row corresponds to the fast-burning flame, while the bottom row shows the buoyant flame. The observed time scales exhibit significant differences. The fast flame reaches the edge of the window within 10 ms after ignition (t_0), while the slow flame crosses the top of the window at 48 ms after ignition at a flame radius of only 1.9 cm. Subsequently, the flame continues to burn and even develops a cusp at the flame front's bottom, a clear indicator of highly buoyant flames (cf. Fig. 3ε).

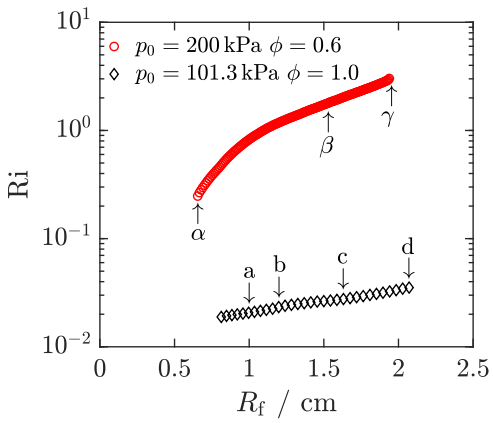

Figure 4: Richardson numbers of the fast-burning flame (black diamonds) and the slow-burning highly buoyant flame (red circles). The latin and greek letters correspond to the images in Fig. 3.

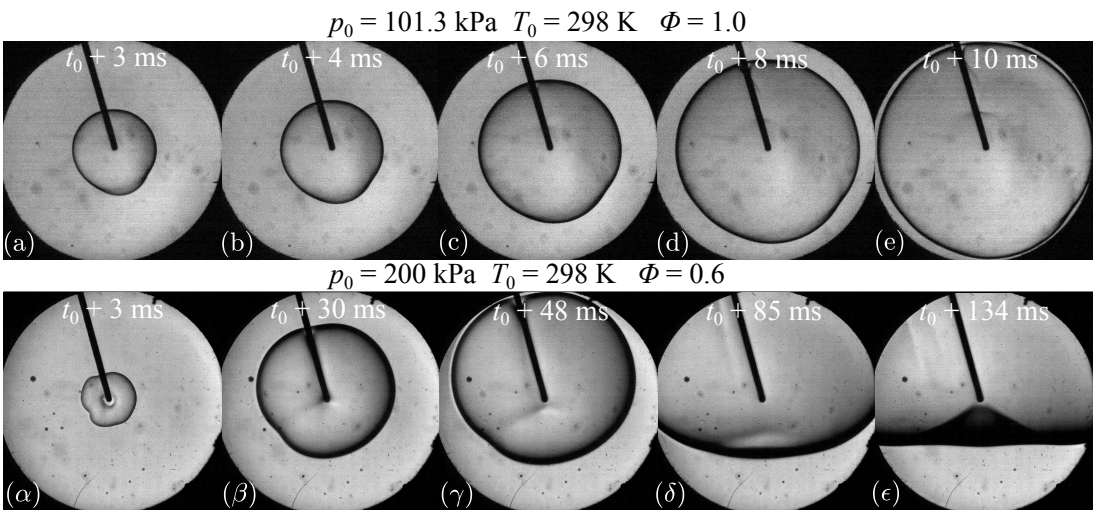

Figure 3: Sequence of Schlieren images of methane/air mixtures at $T_0 = 298\,K$. First row: fast-burning flame with initial conditions $p_0 = 101.3\,kPa$ and $\phi = 1.0$; second row: slow-burning buoyant flame at initial conditions $p_0 = 200\,kPa$ and $\phi = 0.6$.

Fig. 4 displays the respective Richardson numbers of the two cases with increasing flame radius. The Richardson number for the fast-burning flame remains at values far below unity, indicating that gravity-induced buoyancy does not play a role here. In contrast, significantly higher Richardson numbers of up to approximately three are observed for the slow-propagating flame. As the maximum observed flame radius is 1.9 cm, the Richardson number cannot be calculated from the optical measurements beyond this point. Nevertheless, the trend suggests increasing Richardson numbers as the flame radius increases.

Laminar flame speed

Both Schlieren and PIV techniques can be used to determine the instantaneous flame radius. During post-processing of the images, the electrodes are removed and the background is subtracted. The resulting flame contour is filled in to calculate the flame radius using $R_\mathrm{f} = \sqrt{A_\mathrm{f}/\pi}$, where A_f is the flame cross-sectional area. Fig. 5 shows the results for a fast-burning non-buoyant flame. Red circles and black diamonds represent the flame propagation speeds extracted from the Schlieren and PIV methods, respectively. Dotted lines starting from the origin correspond to constant radii. The PIV images have a higher pixel resolution, resulting in a more limited field of view than the Schlieren recordings. As a consequence, the maximum recorded radius is 1.5 cm in the PIV setup, while the Schlieren camera has optical access to the entire window with a diameter of 5 cm. Additionally, the increased pressure decelerates the flame propagation at a flame radius of approximately 2 cm. Therefore, the data beyond this point are excluded. The determination of flame prop-

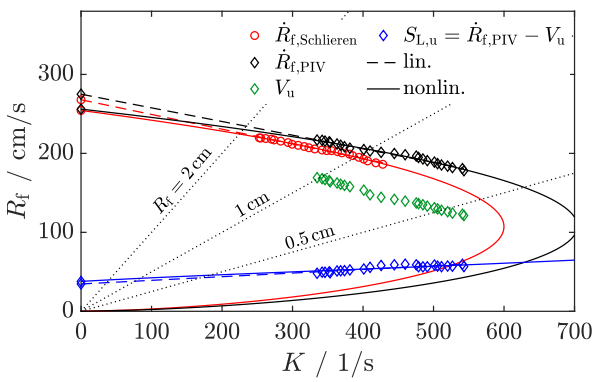

Figure 5: Stretch dependence of flame propagation speed $\dot{R}_\mathrm{f}$, unburned flow velocity ahead of the flame V_u, and the laminar flame speed evaluated in the unburned gas $S_\mathrm{L,u}$ are shown for the fast-burning flame at initial conditions $p_0 = 101.3$ kPa, $T_0 = 298$ K and $\phi = 1.0$.

agation speeds $\dot{R}_\mathrm{f,Schlieren}$ and $\dot{R}_\mathrm{f,PIV}$ involves extracting radii at different iso-temperatures, as reported in previous research [14]. In PIV images, the burned reagion corresponds to an area of evaporated seeding oil particles. The temperature at the outer flame front is equal to the boiling point of the seeding oil of 580 K. Conversely, the Schlieren method locates the flame front at an iso-surface of 840 K [15], closer to the burned region. The linear fit with Eq. 7 is represented by dashed lines, while the solid lines correspond to the nonlinear extrapolation with Eq. 8. The results show that the unstretched laminar flame speeds in the burned region are consistent for both optical methods with $S^0_\mathrm{L,b} = 254$ cm/s. The maximum unburned velocity ahead of the flame front V_u follows a similar trend as the flame propagation speed. The laminar flame speed with respect to the unburned region can be directly obtained from Eq. (2), resulting in a value of 36.5 cm/s when extrapolated to zero stretch. To apply Eq. (10), density ratios between the burned and unburned are determined in equilibrium calculations with Cantera [16]. The unstretched laminar flame speed in the burned $S^0_\mathrm{L,b}$ then yields $S^0_\mathrm{L,u} = 33.8$ cm/s. Therefore, the Schlieren method and PIV produce similar laminar flame speed results for a fast-burning spherical flame.

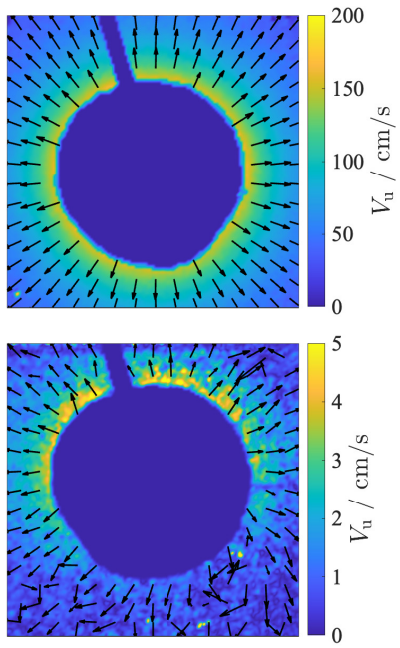

Figure 6: Instantaneous flow field of the spherical fast-burning flame (top) and the slow-burning buoyant flame (bottom).

Fig. 6 shows the velocity fields of the fast and slow-propagating flames. The fast-burning flame exhibits a uniform velocity in the unburned in all directions with nearly constant positive curvature of the circular cross-section. In this case, the assumption of uniform stretch along the flame front is applicable. On the other hand, the cross-section of the slow-burning flame also appears circular with constant positive curvature, but the flow velocity in the unburned region shows local variations. As the flame lifts upward, the flow velocity is considerably higher at the top of the flame, where flame speed and buoyancy act in the same direction. At the bottom of the flame, the flame tries to propagate downward, but buoyancy accelerates the burned gases

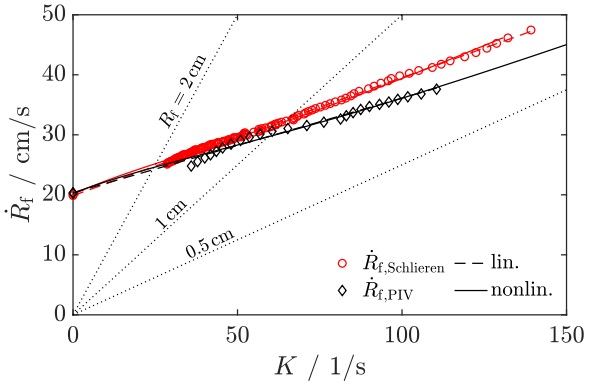

Figure 7: Stretch dependence of flame propagation speed $\dot{R}_f$, unburned flow velocity ahead of the flame V_u and the laminar flame speed evaluated in the unburned gas $S_{L,u}$ is shown for the slow-burning buoyant flame at initial conditions $p_0 = 200\,\text{kPa}$, $T_0 = 298\,\text{K}$ and $\phi = 0.6$.

upward, resulting in very low downward velocities. In addition, the velocity magnitude and direction are scattered due to the low velocity in the bottom region. Minor disruptions induce movement in the particles, leading to a divergence in the directions of their velocity vectors. The low-velocity magnitude also causes a lack of flow stabilization. Due to the absence of a clear singular velocity for the unburned flow ahead of the flame front, only the flame propagation speed is shown in Fig. 7. The Schlieren and PIV-extracted speeds converge toward the same extrapolated unstretched value of approximately 20 cm/s. In contrast to the fast-burning flame, where positive Markstein lengths lead to an increase in flame speed with decreasing stretch K, a negative Markstein length is found for the very lean methane/air mixture. As the curvature is positive, Eq. 7 suggests that the unstretched flame speed $S^0_{L,b}$ should be lower than the stretched flame speed $S_{L,b} = \dot{R}_f$, which is confirmed by the results.

Local Flame Curvature

The buoyant flame has spatially constant instantaneous values for curvature and strain rate, and remains nearly spherical in the range where the entire flame is visible. However, as the experiment progresses, the flame shape strongly diverges from a sphere, stretching in a horizontal direction and forming an inward cusp at the bottom. While this cusp is visible in the Schlieren images, the exact contour cannot be identified. PIV is employed to get a glimpse inside the cusp and identify the flame contour and flow characteristics. Fig. 8 (top) shows an instant of the later stage of the slow-burning methane/air flame, with the background subtracted to ease the identification of seeding particles and the location of the flame front. In the following analysis, a subsection of the flame front is studied in terms of curvature indicated by the red square in the image. Initially, the local curvature of the flame contour is computed. However, the curvature exhibits a high scatter due to the sharp corners in the flame front caused by the image's resolution (cf. Fig. 8 middle). To address this, three regions are defined in the observed flame front region: (1) a region of large positive curvature, (2) a region of low positive curvature, and (3) a region of large negative curvature.

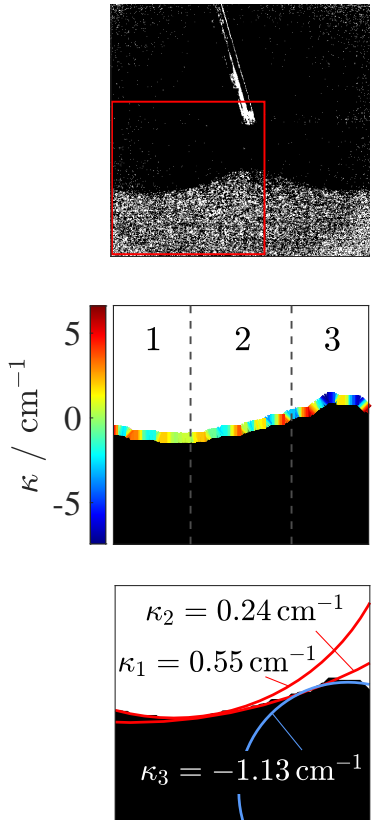

Figure 8: Analysis of flame front curvature for the buoyant methane/air flame at $p_0 = 200\,\text{kPa}$, $T_0 = 298\,\text{K}$ and $\phi = 0.6$. (Top): image corresponds to a background-subtracted PIV image. The red square represents the area of interest investigated for curvature in the middle and bottom figures. (Middle): local curvature on the flame front. Burned gases are white; unburned gases are black. (Bottom): mean curvatures extracted from sections 1, 2, and 3.

The mean curvature is calculated for each region and is represented by the corresponding circle with $r_i = 1/\kappa_i$ in Fig. 8 (bottom). Focusing on the right-hand side of Eq. 9 and assuming a negative Markstein length of curvature $\mathscr{L}_\kappa$, a positive curvature leads to flame acceleration. In contrast, a negative curvature leads to flame deceleration. Hence, in terms of curvature, regions 1 and 2 increase the flame propagation speed, working against the buoyancy-induced lift. The strongly curved region 1 burns faster than the slightly curved region 2. Furthermore, the cusp in the bottom center of the flame has a negative curvature. Negative curvature and a negative Markstein length cause the flame front to decelerate, amplifying the formation of the cusp at the bottom of the flame.

Conclusions

This study experimentally investigated laminar methane/air flames in a constant volume spherical combustion vessel to determine their laminar flame speeds. Two cases with different initial conditions were considered, resulting in a fast-burning spherical flame and a slow-burning flame strongly influenced by buoyancy during flame propagation. The Schlieren method and Particle Image Velocimetry were used to capture flame propagation and oil particle movement in the unburned region. Instantaneous flame radii from Schlieren and PIV images lead to the same unstretched laminar burning velocity in the burned. The laminar flame speed in the unburned was obtained for the fast-burning flame by subtracting the maximum flow velocity ahead of the flame from the flame propagation speed. The unstretched flame propagation speed in the burned region yielded a similar result when multiplied by the density ratio of burned and unburned gases. The slow-burning flame was created by increasing pressure to 200 kPa and diluting with air to an equivalence ratio of $\phi = 0.6$, and was affected by buoyancy, as confirmed by the relatively large Richardson number during combustion. The flame morphology was investigated after an extended period, and local curvature was computed from the flame contour at the bottom of the flame. The positively curved, outward-bulging flame front regions lead to a flame speed increase. In contrast, the negatively curved, inward-bulging regions decelerate the flame front, causing further deformation at the bottom. In our future studies, we plan to explore the impact of strain rate on the deformation of highly buoyant flames, encompassing all stretch-related phenomena. Our objective is to ascertain the Markstein length of curvature $\mathscr{L}_\kappa$ and the Markstein length of strain $\mathscr{L}_{K_S}$ to precisely determine the local laminar flame speed in the vicinity of a buoyant flame. We aim to establish a connection between correcting buoyancy-affected results and determining them in a standard Schlieren setup without requiring information on the flow field.

Acknowledgement

The authors from RWTH gratefully acknowledge the financial support provided by the National Institute of Standards and Technology (NIST), Grant no. 70NANB21H157. Co-authors from NIST obtained financial support under contract DE-EE0007615 from the Office of Energy Efficiency and Renewable Energy, U.S. Department of Energy, and the U.S. Department of Defense, Strategic Environmental Research and Development Program (SERDP), project WP-2740.

References

[1] N. Peters, *Turbulent Combustion* (Cambridge University Press, 2000).

[2] ISO 817: Refrigerants - Designation and Safety Classification, *ISO, Geneva* (2014).

[3] J. Beeckmann, L. Cai, and H. Pitsch, Experimental investigation of the laminar burning velocities of methanol, ethanol, n-propanol, and n-butanol at high pressure, *Fuel* (2014).

[4] R. Hesse, C. Bariki, M. J. Hegetschweiler, G. T. Linteris, H. Pitsch, and J. Beeckmann, Elucidating the challenges in extracting ultra-slow flame speeds in a closed vessel—A CH2F2 microgravity case study using optical and pressure-rise data, *Proc. Combust. Inst.* (2022).

[5] L. Berger, R. Hesse, K. Kleinheinz, M. J. Hegetschweiler, A. Attili, J. Beeckmann, G. T. Linteris, and H. Pitsch, A DNS study of the impact of gravity on spherically expanding laminar premixed flames, *Combust. Flame* (2020).

[6] C. Law and G. Faeth, Opportunities and challenges of combustion in microgravity, *Prog. Energy Combust. Sci.* (1994).

[7] J. Beeckmann, R. Hesse, J. Schaback, H. Pitsch, E. Varea, and N. Chaumeix, Flame propagation speed and markstein length of spherically expanding flames - assessment of extrapolation and measurement techniques, *Proc. Combust. Inst.* (2019).

[8] G. Settles and M. Hargather, A review of recent developments in schlieren and shadowgraph techniques, *Measurement Science & Technology* (2017).

[9] *CBT-120 Datasheet*, Luminus Devices, Inc. (2011).

[10] E. Varea, V. Modica, A. Vandel, and B. Renou, Measurement of laminar burning velocity and Markstein length relative to fresh gases using a new postprocessing procedure: Application to laminar spherical flames for methane, ethanol and isooctane/air mixtures, *Combust. Flame* (2012).

[11] S. M. Candel and T. J. Poinsot, Flame stretch and the balance equation for the flame area, *Combust. Sci. Technol.* (1990).

[12] A. Kelley, J. Bechtold, and C. Law, Premixed flame propagation in a confining vessel with weak pressure rise, *J. Fluid Mech.* (2012).

[13] P. Clavin and J. C. Graña-Otero, Curved and stretched flames: the two markstein numbers, *J. Fluid Mech.* (2011).

[14] G. Giannakopoulos, A. Gatzoulis, C. Frouzakis, M. Matalon, and A. Tomboulides, Consistent definitions of "flame displacement speed" and "Markstein length" for premixed flame propagation, *Combust. Flame* (2015).

[15] D. Dunn-Rankin and F. Weinberg, Location of the schlieren image in premixed flames: Axially symmetrical refractive index fields, *Combust. Flame* (1998).

[16] D. G. Goodwin, H. K. Moffat, I. Schoegl, R. L. Speth, and B. W. Weber, Cantera: An object-oriented software toolkit for chemical kinetics, thermodynamics, and transport processes, `https://www.cantera.org` (2022), version 2.6.0.